Trace element partitioning between type B CAI melts and melilite and spinel: Implications for trace element distribution during CAI formation

C.C. Lundstrom [a,*], A.L. Sutton [a], M. Chaussidon [b], W.F. McDonough [c], R. Ash [c]

[a] *Department of Geology, University of Illinois at Urbana-Champaign, 1301 W Green St, 245 NHB, Urbana, IL 61801, USA*
[b] *CRPG-CNRS, BP 20, 15 rue Notre Dame des Pauvres, 54501 Vandoeuvre-lès-Nancy Cedex, France*
[c] *Department of Geology, University of Maryland, College Park, MD 20742, USA*

Abstract

Calcium- and aluminum-rich inclusions (CAIs), occurring in chondritic meteorites and considered the oldest materials in the solar system, can provide critical information about the environment and time scale of creation of planetary materials. However, interpretation of the trace element and isotope compositions of CAIs, particularly the light elements Li, Be, and B, is hampered by the lack of constraint on melilite–melt and spinel–melt partition coefficients. We determined melilite–melt and spinel–melt partition coefficients for 21 elements by performing controlled cooling rate (2 °C/h) experiments at 1 atmosphere pressure in sealed platinum capsules using a synthetic type B CAI melt. Trace element concentrations were measured by secondary ion mass spectrometry (SIMS) and/or laser ablation inductively coupled plasma mass spectrometry (LA-ICP-MS). Melilites vary only slightly in composition, ranging from $Åk_{31-43}$. Results for the partitioning of trace elements between melilite and melt in three experiments and between spinel and melt in two experiments show that partition coefficients are independent of trace element concentration, are in good agreement for different analytical techniques (SIMS and LA-ICP-MS), and are in agreement with previous measurements in the literature. Partition coefficients between intermediate composition melilites and CAI melt are the following: Li, 0.5; Be, 1.0; B, 0.22; Rb, 0.012; Sr, 0.68; Zr, 0.004; Nb, 0.003; Cs, 0.002; Ba, 0.018; La, 0.056; Nd, 0.065; Sm, 0.073; Eu, 0.67; Er, 0.037; Yb, 0.018; Hf, 0.001; Ta, 0.003; Pb, 0.15; U, 0.001; Th, 0.002. Site size energetics analysis is used to assess isovalent partitioning into the different cation sites. The Young's modulus deduced from +2 cations partitioning into the melilite X site agrees well with the bulk modulus of melilite based on X-ray diffraction methods. The changes in light element partitioning as melilite composition varies are predicted and used in several models of fractional crystallization to evaluate if the observed Li, Be, and B systematics in Allende CAI 3529-41 are consistent with crystallization from a melt. Models of crystallization agree reasonably well with observed light element variations in areas previously interpreted to be unperturbed by secondary processes [Chaussidon, M., Robert, F., McKeegan, K.D., 2006. Li and B isotopic variations in an Allende CAI: Evidence for the in situ decay of short-lived [10]Be and for the possible presence of the short-lived nuclide [7]Be in the early solar system. *Geochim. Cosmochim. Acta* **70**, 224–245], indicating that the trends of light elements could reflect fractional crystallization of a melt. In contrast, areas interpreted to have been affected by alteration processes are not consistent with crystallization models.
© 2006 Elsevier Inc. All rights reserved.

1. Introduction

Ca- and Al-rich inclusions (CAIs) in chondrite meteorites are the oldest crystalline solids in the solar system (Chen and Wasserburg, 1981; Tilton, 1988; Amelin et al., 2002). As a result of this, the trace element and isotopic compositions of CAIs can reveal information about the nature and timing of the processes during the earliest history of the solar system. Despite most CAIs having had complex histories during and after their initial formation (e.g., MacPherson, 2004), sorting out the primary processes of CAI formation remains a major goal of planetary science.

CAIs consist primarily of CaO, Al$_2$O$_3$, SiO$_2$, MgO, and TiO$_2$ (CMAS + Ti), consistent with being either high temperature condensates from a gas of solar composition or evaporative residues. Type B CAIs (Grossman, 1975), a class of coarse-grained CAIs often interpreted to reflect crystallization from a melt, contain mostly melilite (Ca$_2$(Al,Mg)(Si,Al)$_2$O$_7$), Ti-rich clinopyroxene, plagioclase, and spinel (MgAl$_2$O$_4$) as primary phases. Spinel crystallizes first in type B CAI material (Stolper and Paque, 1986) but usually remains proportionally small throughout the crystallization sequence. Melilite is a solid solution between the endmember components *gehlenite* Ca$_2$Al(AlSi)O$_7$ and *åkermanite* Ca$_2$MgSi$_2$O$_7$. Being the modally dominant phase of CAIs, melilite is a major control on the bulk and trace element distribution within CAIs.

The trace element chemistry of melilites and spinels in CAIs can reveal key information about the processes of CAI formation including the role of volatilization, fractional condensation, and fractional crystallization. However, assessment of how type B CAIs crystallized from a melt requires knowledge of the appropriate mineral–melt partition coefficients. For example, Mason and Martin (1974) interpreted rare earth element (REE) patterns of coexisting melilites and pyroxenes from some Allende CAI to reflect crystallization from a melt based on inferred partitioning behavior between these phases. Similarly, forsterite bearing type B3 CAIs have been interpreted to reflect crystallization from molten evaporative residues (Wark et al., 1987). On the other hand, measured melilite–melt partition coefficients (Beckett et al., 1990) have been used to conclude that trace element distributions within an Allende type B1 CAI (zoned with melilite-rich mantles) could not solely reflect equilibrium partitioning with a melt (Kennedy et al., 1997). Davis et al. (1996) measured melilite–melt partition coefficients at different cooling rates in order to explain REE systematics within three Allende CAI; the faster cooling rate experiment results could not explain the observed REE contents nor the REE patterns. MacPherson and Davis (1993) noted systematic changes in melilite Na content to infer a multiple evolution history; this led to recent work examining Na partitioning between melilite and CAI melt (Beckett and Stolper, 2000; Beckett et al., 2000). Trace element partitioning between other phases and CAI melt has also contributed to understanding CAI formation. Simon et al. (1991) inferred partition coefficients for fassaite during formation of zoned fassaites within type B CAI from Allende, reproducing observed trends by models of fractional crystallization. Lastly, petrogenetic information on CAI genesis has been provided by Ti, V, and Fe contents in spinel (Connolly et al., 2003). These studies all illustrate the need for improved constraint on the relevant mineral–melt partition coefficients that control the element distribution within CAIs.

Recent isotopic studies have emphasized the behavior of the "light elements" Li, Be, and B during CAI formation processes due to the possibility that traces of now extinct short-lived radionuclides ^{10}Be (which decays to ^{10}B with $t_{1/2} = 1.52$ My) and ^{7}Be (which decays to ^{7}Li with $t_{1/2} = 53$ days) may have been incorporated into CAIs (McKeegan et al., 2000; Sugiura et al., 2001; Chaussidon et al., 2004; Chaussidon et al., 2006). ^{10}Be and ^{7}Be differ from other previously identified short-lived radionuclides such as ^{26}Al (which decays to ^{26}Mg with $t_{1/2} = 0.73$ Ma, Lee et al., 1976) because both the parent and daughter isotopes are trace elements in the CAIs occurring at ng/g to μg/g concentrations. Furthermore, ^{10}Be is largely produced by spallation reactions within the solar nebula, although Desch et al. (2004) have suggested it may have been produced in the interstellar medium prior to solar system formation. Because the abundance of an original short-lived nuclide can be determined based on the slope of an isochron (e.g., ^{10}B/^{11}B versus ^{9}Be/^{11}B for ^{10}Be), the accuracy of this determination depends primarily on the range of the parent/daughter fractionation present in the CAIs and thus how these elements partition between CAI minerals.

The search for signatures of ^{10}Be and ^{7}Be was initiated by previous experimental work which showed that Be can be either incompatible or compatible in melilite, depending on the melilite composition (Beckett et al., 1990). Assuming B to be incompatible in melilite (which might be expected given its small size relative to the mineral forming cations), significant Be–B variations in melilites should be present. The incorporation of ^{10}Be in CAIs has now been demonstrated for several type B CAIs (McKeegan et al., 2000; Sugiura et al., 2001; MacPherson et al., 2003) with Be–B in melilite varying by over two orders of magnitude. However, it has not been clearly demonstrated yet that the range in Be–B observed reflects fractional crystallization of a CAI melt because the melilite–melt partition coefficient for B has yet to be determined. Thus, the relative ability of magmatic processes to fractionate B–Be compared to secondary redistribution during re-heating events and/or alteration is not yet known. The similar lack of constraint on Li partitioning severely hinders interpretations of ^{7}Be systematics. Knowledge of the mineral–melt partitioning of Li is crucial in order to: (i) predict the behavior of Li relative to Be during the crystallization of a CAI melt and assess the differences in Be–Li between different minerals; and (ii) identify zones in the CAIs where the Li and Be distribution has not been disturbed by post-magmatic processes, providing robust isochrons between ^{7}Li/^{6}Li and ^{9}Be/^{6}Li (Chaussidon et al., 2004; Chaussidon et al., 2006). Due to the extremely short half life of ^{7}Be and the high diffusivity of Li in crystals (e.g., Gilletti and Shanahan, 1997), the ^{7}Be isochron is particularly sensitive to perturbations occurring after crystallization. Because the possible incorporation of ^{7}Be into CAIs has strong implications for the irradiation history of the early solar system and the origin of CAIs (see Chaussidon and Gounelle, 2006), experimental determination of Li partitioning between melilite, spinel, and CAI melt is critically required.

Despite the need for constraints on melilite–melt partitioning, few experimental studies have been conducted on the melilite–CAI melt system. Kuehner et al. (1989), determined partition coefficients between melilite and melilite melt for Sr, Y, Zr, La, Sm, and Yb in Åk$_{12-90}$ (mole

fraction of Åkermanite in melilite). Beckett et al. (1990) determined partitioning for Be, Sc, Ba, La, Ce, and Tm between melilite of $\mathring{A}k_{25-75}$ and a type B CAI composition melt. Beckett et al. (2000) also measured Na partitioning between melilite and similar CAI melt. Ryerson et al. (2005) have also recently reported new results for melilite, anorthite, and clinopyroxene–CAI melt partitioning. Here, we present new melilite–CAI and spinel–CAI melt partition coefficients in the CMAS + Ti system for a large set of trace elements (Li, Be, B, Rb, Sr, Zr, Nb, Cs, Ba, La, Ce, Nd, Sm, Eu, Er, Yb, Hf, Pb, Th, and U). These data are then used to evaluate the site size energetics of element substitution into melilite and to assess possible scenarios for Li–Be–B concentration variations within CAIs, placing constraints on the element distribution processes and the chronology of CAI formation.

2. Methods

The starting material for this study, based on that used in Beckett et al. (1990), was synthesized from a mixture of ALFA Puratronic MgO, Al_2O_3, SiO_2, $CaCO_3$, and TiO_2 and has a bulk composition similar to average type B CAI (Table 1) (Wark, 1979). After grinding by hand in an agate mortar under ethanol, the starting material was decarbonated at 1000 °C, melted in air in a Pt crucible at 1550 °C overnight, and quenched to glass. After grinding to a fine glass powder, splits of this material were taken to make trace element enriched powders while the undoped powder was put aside as a dilution agent. To make the doped powder, aqueous nitrate solutions of the trace elements Li, Be, B, La, Sm, Er, Yb, Nb, Hf, and Zr and chloride solutions of Rb, Cs, Ba, and Co were added to produce ~500 ppm concentrations, ground in agate, denitrified at ~540 °C for ~6 h, and reground a final time. Some differences in doping occurred at different times and between different splits: for instance, Rb and Cs were added to the enriched powder used for experiment 2.6.28.H in order to increase the concentrations of these elements in the melt and allow measurement of D_{Rb} and D_{Cs}.

Experiments were performed in sealed platinum capsules in a Deltech VT-31 furnace with temperature measured using a Pt/Pt-10%Rh thermocouple (type R). The thermocouple calibration was checked relative to the melting point of Au and diopside. To perform the partitioning experiments, the undoped and doped starting materials were ground together in appropriate proportions to obtain powders having ~5, ~50 and ~500 ppm trace elements (corresponding to L, M, and H, respectively). Each mixture (~20–40 mg) was then added to a ~10 mm long, 3 mm diameter Pt capsule. Each capsule was dried open for ⩾12 h at 110 °C and then sealed by welding. Capsules that leaked melt during the run were not used for analysis as elements volatile in air, especially Li, could have escaped.

The L, M, and H capsules were run together in the furnace by holding at the highest temperature (T_{max}) for a set time period and cooling at 2 °C/h to a final temperature lower than the melilite crystallization temperature (Fig. 1 and Table 2). This cooling rate is similar to the likely cooling rate of natural CAIs (Stolper and Paque, 1986; Beckett et al., 1990). The final temperatures were intended to be just below the melilite-in temperature under the conditions of these experiments. Table 2 gives run conditions for those experiments that were analyzed for trace elements. Since all of the 5 ppm (L) trace element doped charges either leaked during their runs or did not crystallize melilite, no partitioning results at this doping level are presented. Run products were mounted in epoxy and polished as flat surface mounts.

Phase identification was done using backscattered electron imaging on a JEOL 840A scanning electron microscope (SEM) in the Department of Geology at UIUC. The similar indices of refraction for melilite and glass make it difficult to distinguish these phases petrographically. Because the CaO content represents the greatest compositional difference between melilite and melt, melilite grains were most easily identified using Ca or Si X-ray maps. Major element compositions of phases were determined by two different methods. The first involved wavelength dispersive X-ray analysis on the Cameca SX50 electron microprobe at the University of Chicago using ~2 μm beam, accelerating voltage of 15 kV, and beam current of 30 nA. The second method used standards based energy dispersive X-ray analysis on the JEOL 840A SEM using a 10 nA beam and a 15 kV accelerating voltage. There is good agreement between the two

Table 1
Major oxide concentrations (wt%) of experimental starting glass, starting glass of Beckett et al. (1990), and average Type B CAI

	CaO	MgO	Al_2O_3	SiO_2	TiO_2	total
CAI-glass[a]	29.4	9.0	26.6	33.1	1.3	99.4
Beckett[b]	28.5	9.0	26.4	32.2	1.1	97.2
Wark[c]	28.9	10.3	28.5	29.6	1.3	98.6

[a] Analysis by electron microprobe (WDS).
[b] Starting glass of Beckett et al. (1990).
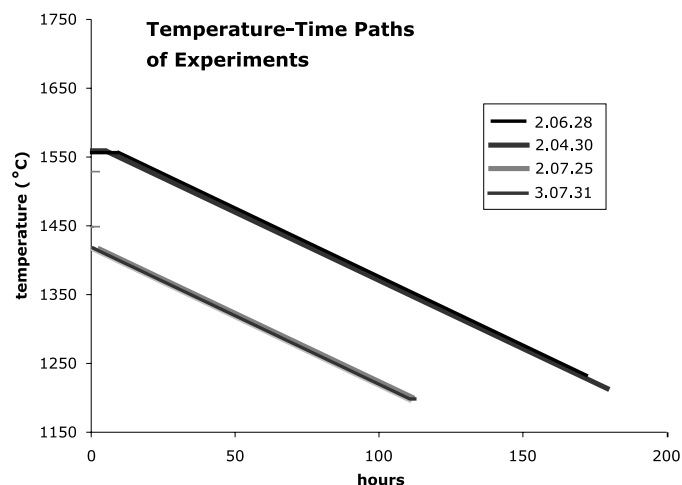[c] Average Type B CAI (Wark and Lovering, 1982).

Fig. 1. Temperature–time paths of experiments.

Table 2
Experimental conditions and results

Sample	T_{max} (°C)	Time at T_{max} (h)	T_{quench} (°C)	Time at T_{quench} (h)	Phases	Modal abundances			Ave. Mel. Comp.
						Gl	Sp	Mel	
2.04.30.H	1560	5	1213	0	gl + sp + mel	66	10	24	Åk$_{38}$
2.07.25.H	1420	3	1200	0	gl + sp + mel	80	13	8	Åk$_{44}$
3.07.31.M	1420	1	1199	2	gl + sp + mel	59	11	30	Åk$_{41}$
2.6.28.H	1560	10	1225	0	gl + sp	90	10		

Cooling rates in all experiments occurred at 2 °C/h. Glass, gl; melilite, mel; spinel, sp.

methods. Standards included MgO; anorthite for CaO, Al$_2$O$_3$ and SiO$_2$; and rutile for TiO$_2$. Mineral modes of the experiments were determined from the major element data using mass balance and a least squares fitting technique (Table 2).

Reported trace element concentrations and partition coefficients reflect averages of at least two (but up to 6) separate analysis spots in each phase (glasses and minerals) for both SIMS and LA-ICP-MS. The Li, Be, and B concentrations were measured using the Cameca ims-3f ion microprobe (SIMS) located at the CRPG-CNRS (Nancy, France). A primary beam of negative oxygen ions (20 nA) was accelerated at 10 kV to a sample spot of ~10–20 μm width and secondary ions were extracted at 4400 V. Standard energy filtering techniques were used (Shimizu et al., 1978) with ion intensities ratioed to Si or Al (spinel) with accuracy estimated at ±20%. A technical problem with magnet positioning was noted well after the analysis session for sample 2.07.25.H resulting in an accuracy bias for element concentrations; therefore we do not report SIMS concentrations for this experiment. However, because the bias applies to both melilite and glass analyses, the measured partition coefficients for this session are thought to be accurate and are reported.

All other trace element concentrations along with Li, Be, and B were measured using the Finnigan Element 2 ICP-MS coupled to either a New Wave 193 nm excimer or 213 nm quintuple coupled Nd-YAG laser at the University of Mary-land. Spot size was generally ~20–40 μm except for spinel analyses in which a 100 μm spot was used. Analyses consisted of coupled magnetic and electrostatic scans during which ~20 s of background counts were obtained with the laser off followed by collection of the ablation signal; concentration data were extracted by selecting a 10–20 s steady plateau of counts during the ablation. Ion intensities were ratioed to Si or Ti (spinel) and calibration was performed relative to NIST610 with two standard BCR-2 runs in every session. In addition to the trace elements formally doped into the experiment, Sr, Zr, Nd, Pb, Th, and U concentrations were also measured with accuracy estimated at ±10% excepting lower concentration analyses.

3. Results

We report the results of three experiments that produced euhedral melilites suitable for melilite–melt partition coefficient determinations and two experiments suitable for determining spinel–melt partition coefficients (Tables 3 and 4). All reported results represent successful experiments which grew euhedral crystals coexisting with homogeneous quenched melts (glass) in which there was no evidence for leaking of the platinum capsule. Fig. 2 shows BSE and X-ray map images of a representative experiment.

The major element compositions of the phases in each experiment are given in Table 3. Glass homogeneity is indicated by the standard deviation of multiple (10) spot anal-

Table 3
Major element compositions (wt%) of glass, melilite, and spinel

Expt.	Phase	Method	CaO	MgO	Al$_2$O$_3$	SiO$_2$	TiO$_2$
2.04.30.H	Glass	EDS	29.24	7.16	21.95	39.79	1.87
	Glass	WDS	29.81	7.06	21.95	39.13	1.96
	Mel-An38	WDS	41.16	5.67	22.37	30.75	0.06
	Spinel	EDS		27.25	72.62		0.10
2.07.25.H	Glass	EDS	33.40	5.98	20.78	38.42	1.41
	Glass	WDS	33.02	6.12	20.54	38.70	1.64
	Mel-An44	EDS	40.18	5.81	22.76	31.20	0.03
	Mel	WDS	41.02	6.43	20.20	32.39	0.04
3.07.31.M	Glass	EDS	29.20	6.75	22.06	40.03	1.95
	Mel-An41	EDS	40.67	5.96	20.59	32.74	0.05
2.06.28.H	Glass	EDS	32.93	6.50	21.91	37.32	1.34
	Spinel	EDS		27.25	72.70		0.05

Estimated errors based on sample standard deviation ($n = 3$–10) are ±1% relative for CaO, MgO, Al$_2$O$_3$, SiO$_2$, and ±2% for TiO$_2$. EDS: energy dispersive analysis; WDS: wavelength dispersive analysis.

Table 4
Trace element composition of phases and mineral–melt partition coefficients

	2.6.28.H			2.04.30.H				
	Glass (ppm)	Spinel (ppm)	Spinel–melt D	Glass (ppm)	Mel (ppm)	mel/mel D	Spinel (ppm)	Sp–melt D
	(LA-ICPMS)			(SIMS)				
Li	408 (12)	75 (7)	0.184 (8)	317 (60)	152 (10)	0.48 (7)	32 (3)	0.10 (2)
Be	592 (3)	41 (16)	0.069 (2)	473 (94)	416 (20)	0.88 (7)	19 (2)	0.040 (4)
B	418 (6)	17 (12)	0.05 (4)	335 (66)	550 (12)	0.15 (6)	1.0 (2)	0.003 (1)
Rb	6 (2)							
Sr	34 (5)							
Zr	7 (1)	0.010 (3)	0.0014 (36)					
Nb	532 (12)	0.022 (4)	0.00004 (1)					
Cs								
Ba	492 (16)							
La	581 (16)	0.002 (2)	3×10^{-6} (4)					
Ce								
Nd	583 (16)	0.02 (1)	0.00003 (4)					
Er	494 (8)	0.13 (1)	0.0003 (1)					
Hf	506 (4)	0.50 (5)	0.0010 (1)					
Ta	17 (1)	0.002 (2)	0.0001 (1)					
Pb	1 (1)							
Th	3 (1)	0.002 (1)	0.0006 (4)					
U	7 (1)	0.002 (1)	0.0003 (2)					

	3.07.31.M			2.07.25.H				BCR-2G
	Glass (ppm)	Mel. (ppm)	Mel/melt D	Glass (ppm)	Crystallinity[a]	Mel. (ppm)	Mel/melt D	(ppm)
Li (SIMS)	36 (6)	22 (4)	0.62 (12)				0.50 (9)	
Li (LA)	54 (7)	23 (4)	0.4 (2)	389 (14)		171 (8)	0.44 (3)	
Be (SIMS)	23 (4)	25 (4)	1.10 (20)				1.1 (1)	
Be (LA)	32 (2)	31 (3)	0.98 (9)	493 (19)		519 (20)	1.05 (6)	
B (SIMS)	170 (34)	30 (6)	0.17 (4)				0.21 (5)	
B(LA)	226 (6)	59 (5)	0.26 (2)	527 (30)		137 (10)	0.26 (2)	
Rb	81 (1)	1.2 (1)	0.015 (2)	1070 (38)		11 (1)	0.010 (2)	72
Sr	25 (1)	18 (1)	0.72 (2)	27 (1)		18 (1)	0.64 (2)	467
Zr	15 (1)	0.06 (3)	0.004 (2)					245
Nb	75 (1)	0.38 (8)	0.005 (1)	767 (20)	68%	0.8 (3)	0.0010 (4)	15
Cs	87 (1)	0.44 (1)	0.005 (1)	1190 (60)		1.1 (5)	0.0009 (4)	
Ba	63 (1)	1.1 (1)	0.018 (1)	714 (27)	68%	13 (1)	0.018 (1)	908
La	73 (1)	3.8 (7)	0.052 (1)	806 (24)	72%	46 (6)	0.06 (1)	36
Ce	0.2 (2)	0.008 (1)	0.053 (2)					73
Nd	0.4 (1)	0.020 (2)	0.051 (6)	779 (26)	74%	65 (12)	0.08 (2)	41
Sm	61 (4)	4.5 (5)	0.073 (1)	3.8 (1)	76%	0.27 (1)	0.071 (4)	10
Eu	0.2 (4)	0.014 (1)	0.064 (6)	2.5 (1)	82%	0.17 (1)	0.069 (3)	3
Er	52 (2)	1.77 (6)	0.034 (1)	702 (28)	71%	27 (4)	0.039 (9)	5.3
Yb	57 (2)	0.97 (5)	0.017 (1)	5.1 (1)	64%	0.1 (1)	0.02 (2)	4.2
Hf	54 (2)	0.11 (5)	0.002 (1)	849 (38)	60%	0.4 (2)	0.0005 (2)	6.7
Ta	4 (3)	0.013 (3)	0.003 (1)					
Pb	4.7 (3)	0.71 (7)	0.15 (2)	11.1 (6)		5.5 (5)	0.5 (4)	18
Th	1.3 (1)	0.001 (1)	0.001 (2)	6.4 (3)		0.017 (6)	0.003 (1)	7.9
U	2.5 (2)	0.005 (5)	0.002 (3)	11.3 (3)		0.007 (7)	0.001 (1)	2.5

[a] Based on change in glass composition relative to experiment 2.6.28.H. see text.

yses which is comparable to the internal counting statistics errors for the major element analysis (~1% error). Analyses of the glass adjacent to crystal faces in all experiments, even those quenched immediately to the termination of the temperature ramp, showed no discernible deviation from the average glass composition, implying that diffusion of elements from the melt to the growing crystal was not a limiting factor in the distribution of elements between the crystals and melt.

Our original intention, to grow all crystals directly from a homogeneous melt, led to difficulties in successfully crystallizing melilite, reflecting crystal nucleation problems pre-

viously discussed by Stolper and Paque (1986). Several initial experiments which held the charge above the spinel liquidus at 1560 °C for several hours resulted in failure to crystallize melilite despite dropping the temperature >200 °C below the reported melilite-in temperature of 1400 °C (Stolper, 1982). Experiment 2.6.28.H (Table 2) represents one of these early attempts which crystallized large euhedral spinels but not melilite. Notably, the experiment held at T_{max} (1560 °C) for the shortest duration (~5 h), 2.04.30.H, was the only one of these early experiments to successfully grow melilite (200–500 μm wide euhedral crystals).

The presence or absence of melilite in these early experiments depended primarily on three factors: the maximum temperature (T_{max}) of the run, the time spent at T_{max}, and the final temperature of the run. Although our observed melilite-in temperature (∼1215 °C) was much lower than the ∼1400 °C reported by Stolper (1982) for a similar bulk composition, our melilite-in temperatures are consistent with Stolper and Paque (1986), after taking into account T_{max}, the length of time at T_{max}, and the cooling rates of our experiments. While growing spinel from homogenous melts in experiments 2.4.30.H and 2.6.28.H did allow determination of spinel–melt partition coefficients, the inability to reliably grow melilite from the homogenous melt hindered the primary purpose of this work, determining melilite–melt partitioning. Therefore, we subsequently altered our procedure by lowering the initial temperature of the experiment (T_{max}) to below the "spinel-in" temperature, following the method of Beckett et al. (1990) (Fig. 1). Using the lower T_{max} resulted in many small (∼10 μm) euhedral, instantaneous growth spinels unsuitable for determining spinel–melt partitioning. Although complete homogeneity of the entire charge was not attained using this lower T_{max}, melilite in these experiments should have grown from a well-homogenized melt. Two ∼mm long laser ablation transects across the glass in experiment 2.6.28.H indicate trace element homogeneity in the glass confirming this assumption and providing constraint on the trace element concentration of the CAI melt prior to any melilite crystallization. Subsequent experiments using a lower T_{max} resulted in 100–500 μm melilites in experiments 2.07.25.H and 3.07.31.M. The small spinel grains in these experiments were distributed in irregular zones, mostly likely reflecting settling during the experiment. Some of the melilite grew within these spinel-rich areas but many melilites were free of spinel grains, providing for melilite analyses free of incorporated spinel.

All of these experiments had similar degrees of crystallization and produced relatively unzoned melilites of similar composition (Table 3). For instance, charge 2.04.30.H produced a melilite composition of $\mathring{A}k_{38\pm5}$ (reflecting more than 50 analyses), charge 2.07.25.H produced $\mathring{A}k_{44\pm5}$ while charge 3.07.31.M produced $\mathring{A}k_{41\pm5}$. There was generally no systematic zoning in any of the melilites. For instance, combined backscattered electron (BSE) and X-ray maps (Fig. 2) along with a spot analysis transect across a ∼100 μm wide melilite indicate a subtle bimodal transition rather than a rim-core-rim zonation. Similar BSE images of melilites in all three experiments indicate no major zoning nor any evidence for sector zoning. Finally, the agreement between the modes of different experiments (Table 2), as well as the fit to the individual mass balance mode determinations, indicates that the solid phases present are relatively homogeneous. Notably, despite the differences in crystal growth procedure, the spinel mode between the different experiments is essentially identical and similar to the modes reported in Stolper (1982) for this composition. For example, experiments which started from a homoge-
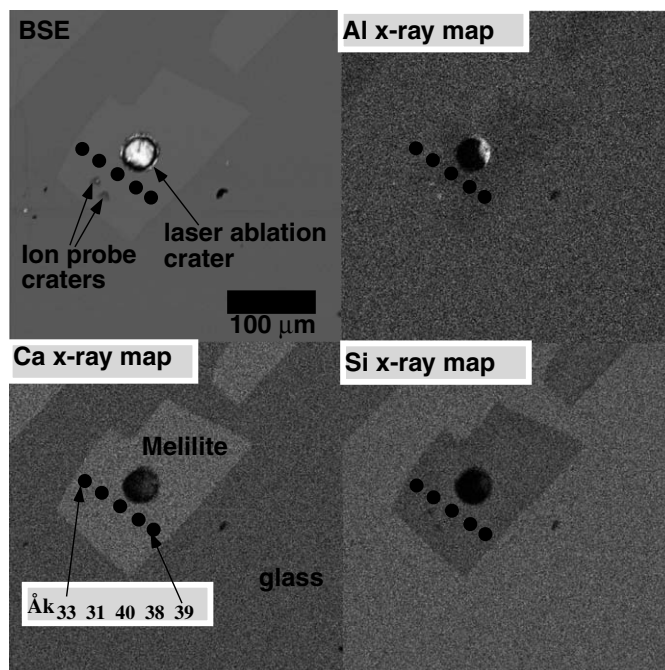

Fig. 2. Backscattered electron image (BSE) of melililte and glass from experiment 2.7.25.H. Note laser ablation crater and SIMS craters. Lighter crystals are melilites while darker gray matrix is glass. Ca and Al X-ray maps indicate little zoning through the crystal. Analysis transect shows relatively minor compositional variations across the crystal.

nous melt (2.4.30.H and 2.6.28.H) grew a few large spinels while the lower T_{max} experiments produced many small (10 μm) euhedral spinels, resulting in the same modes despite differences in growth rate and morphology.

The homogeneity of the melilites in these experiments contrasts with the dynamic crystallization experiments of Beckett et al. (1990) in which average melilite compositions ranged from $\mathring{A}k_{30}$ to $\mathring{A}k_{67}$ and compositions varied from $\mathring{A}k_{25}$ to $\mathring{A}k_{75}$ within large single crystals (500–1000 μm in size) in a predictable fashion from core to rim. More recent experiments by Beckett and Stolper (2000) report similar zoning of melilites. This difference in melilite compositional morphology from our results is somewhat surprising considering that all studies used similar bulk compositions, cooling rates and total amounts of cooling. One possible explanation for the difference between this study and these previous studies might be our use of sealed platinum capsules compared with platinum loops in the previous work (Beckett et al., 1990; Beckett and Stolper, 2000). The greater surface area of the platinum capsules could provide more sites for nucleation, resulting in more numerous, but smaller crystals with less zoning in our experiments relative to those in these previous studies.

The importance of nucleation in growing crystals from this bulk composition is further highlighted by our observation of an anomalous repeated pattern of the higher concentration charge in a set (the 500 ppm charge of the H, M, and L set) crystallizing melilite while lower concentration samples did not. Based on this observation, we hypothesized that the trace element doped powder held the major-

ity of the possible melilite nucleation sites resulting in melilite nuclei in the higher concentration experiments being more likely to survive the T_{max} step. We resolved this problem by growing melilite seed crystals from the base glass powder and adding a small number of these seeds (as finely ground powder) to each of the remaining experiments. When running experiments using melilite seed crystals, the effect of trace element doping level controlling the presence of melilite disappeared. Experimental run 3.07.31 (as well as an unreported experiment which leaked, 3.04.30) produced melilite in all three samples, supporting our initial hypothesis.

Trace element concentrations in the glass, melilite, and spinel and melilite–melt and spinel–melt partition coefficients are given in Table 4. The uncertainty on partition coefficients given reflects the combined errors on glass and crystal analyses. Trace element homogeneity in all of the glasses is indicated by the standard deviation of these analyses which generally averaged ~5% (1σ) for each trace element, consistent with 5–10% precision of the LA-ICP-MS analyses. The light elements Li, Be, and B have larger standard deviations reflecting both counting statistics (LA-ICP-MS) and general reproducibility of concentration analysis of these elements. Trace element concentrations in the melilites or spinel show more variation than in the glass due to uncertainties in counting statistics, reflecting the low concentrations of most of these elements within these phases. No discernible relationship between melilite major element composition and trace element analysis of a particular crater is apparent, consistent with the relatively small variation in major element composition of the melilites in these experiments.

4. Discussion

4.1. Assessment of equilibrium and comparison with previous results

The agreement between the measured melilite–melt partition coefficients for a given element from the three experiments (2.04.30, 2.07.25, and 3.07.31) is excellent (Table 4, Fig. 3). Melilite–melt partition coefficients determined by SIMS versus LA-ICP-MS agree within estimated analytical error. Concentrations show a slight bias between methods (Fig. 4), possibly reflecting uncertainties associated with the yields in the iron-free CAI composition relative to the standards used, but are close to agreement within errors. Because useful yields for the glass and melilite analyses likely differ by <10% (Botazzi et al., 1992), the partition coefficients for a given experiment should be accurate; this is indicated by the good agreement between partition coefficients determined using different methods and from distinct experiments. Finally, although the spinel–melt partition coefficients between different methods and experiments are in good agreement, it should be emphasized that yields from the spinel matrix could be quite different from those in the silicate standards used for calibration and this
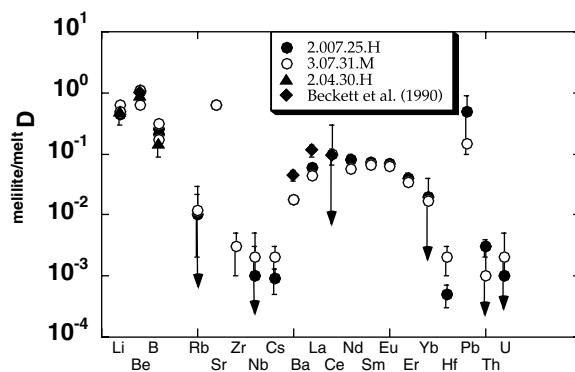

Fig. 3. Melilite–melt partition coefficients from this study and those determined by Beckett et al. (1990) for melilites of Åk$_{38}$ composition. Note the overall good agreement between the different experiments and the results of Beckett et al. (1990). Down pointing arrows reflect errors that result in the minimum partition coefficient being indistinguishable from zero.
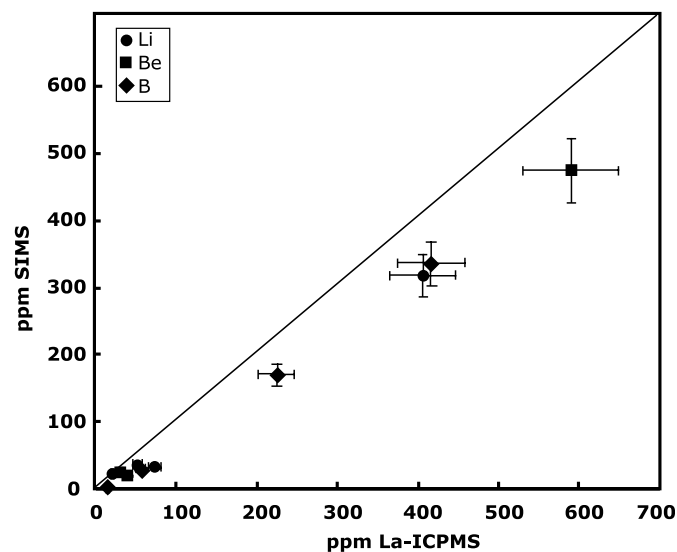

Fig. 4. Comparison of concentration measurements by LAICPMS and SIMS using data for experiment 3.07.31M (measured by both techniques) and comparing experiments 2.04.30.H and 2.6.28.H which used the same glass starting material but had slightly different degrees of crystallization.

could possibly result in systematic biases in the measured spinel–melt partition coefficients; the $^{spinel-melt}D_B$ results from two experiments are different although both indicate considerable incompatibility (Fig. 5).

Although we have not directly assessed equilibrium through a reversal experiment, several observations argue that our measured partition coefficients represent equilibrium values. First, our experiments resulted in euhedral melilites and spinels within a homogeneous glass matrix. Major element analyses of the glass even within a few μm of crystal faces found no inhomogeneity despite quenching of the melt immediately upon reaching the final temperature after cooling (in three out of four experiments). Second, the major element zoning within the melilite crystals is minor; this can be seen by the element
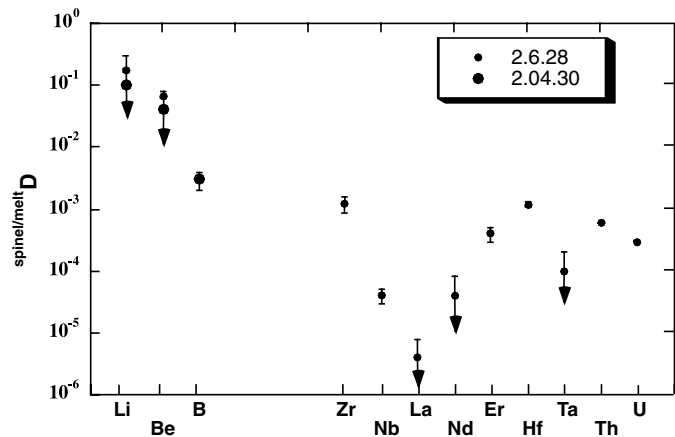
Fig. 5. Spinel–melt partition coefficients from this study. Down pointing arrows reflect errors that result in the minimum partition coefficient being indistinguishable from zero.

X-ray map observed in Fig. 2 and by the relative homogeneity of the major and trace element analyses within the crystal. Finally, as explained below, our measured partition coefficients are generally lower than previous studies. As both analytical and experimental problems will generally lead to partition coefficients that are biased toward values closer to 1, our low partition coefficients for incompatible elements argues for a close approach to equilibrium in our experiments.

Comparison of our results at different doping levels in the melt argues that partitioning occurred within the Henry's Law regime (Fig. 6). The trace element doping level in experiment 3.07.31M was a factor of 10 smaller than the other two experiments, yet all experiments produced nearly identical partition coefficients. Indeed, the only significant deviations occur for elements that have concentrations near detection limits in melilite due to their incompatibility. These results suggest that no deviation from Henry's Law occurred in these experiments (Fig. 6), consistent with
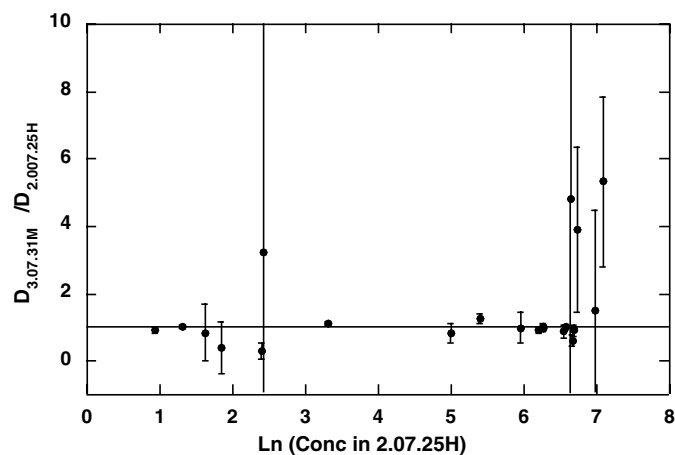

Fig. 6. Variation in the ratio of the melilite–melt partition coefficients between experiments 3.07.31.M and 2.07.25.H for all trace elements measured as a function of trace element concentration in the higher concentration melt. As can be seen, almost all of the elements have ratios within error of one, indicating Henry's Law behavior.

several previous experimental partitioning studies demonstrating Henrian behavior occurs even at total trace element doping levels several times higher than those used in these experiments (e.g., Watson, 1985).

The melilite–melt partition coefficients from this study compare well to those determined by Beckett et al. (1990) for Be, Ba, and La at similar melilite compositions. For instance, the average melilite–melt partition coefficient for Be determined here is 1.02, compared with $^{mel/melt}D_{Be} = 0.79(23)$ and 1.01(28) determined for $Åk_{38}$ and $Åk_{43}$, respectively (Beckett et al., 1990). Partition coefficients for Ba and La ($^{mel/melt}D_{Ba} = 0.018(1)$, $^{mel/melt}D_{La} = 0.052(1)$) are lower than those for similar composition melilites in Beckett et al. ($^{mel/melt}D_{Ba} = 0.038$–0.045, $^{mel/melt}D_{La} = 0.146$–0.114, for melilite variation noted above). One reason for the difference in results could be the distinct difference in crystal zoning between the two studies and the necessity of correcting measured partition coefficients for Åk zoning in the Beckett et al. (1990) study. Both deviations from equilibrium during crystal growth (crystal growth with boundary layer development) or analytical bias (e.g., sampling glass inclusions in a melilite analysis) tend to result in the partition coefficients biased to values closer to one; therefore, the lower partition coefficients from this study may suggest more accuracy, although unknown compositional controls on melilite–melt partitioning or other factors may explain this difference. For instance, inadvertent analysis of small spinel grains could affect our measured partition coefficient and bias the results; however, the constancy of signals during the laser analyses indicate that this problem did not occur during these analyses.

Two other abstracts describe comparable melilite–CAI melt partitioning results to those here. Davis et al. (1996) measured partition coefficients for the REE between CAI melt and melilite in experiments which varied cooling rates between 2 °C/h and 75 °C/h. Although their melilite compositions bracketed our compositions here ($Åk_{23}$ to $Åk_{63}$), their melilite–melt coefficients were generally higher with $^{mel/melt}D_{La} = 0.3$ in $Åk_{23}$ melilite and $^{mel/melt}D_{La} = 0.06$ in $Åk_{63}$ melilite. The REE pattern agrees with our results with the peak in $^{mel/melt}D_{REE}$ occurring around Nd. Ryerson et al. (2005) have recently reported new experimental determinations of Li–Be–B partitioning between melilite and CAI melt which also appear to agree with our results. For $Åk_{50}$ melilite, they find $^{mel/melt}D_{Be}$ of 0.75, $^{mel/melt}D_{Li}$ of 0.45, and $^{mel/melt}D_{B}$ of 0.19 while for $Åk_{100}$ melilite, they find $^{mel/melt}D_{Be}$ of 0.55, $^{mel/melt}D_{Li}$ of 0.53, and $^{mel/melt}D_{B}$ of 0.05.

Kuehner et al. (1989) determined partition coefficients between melilite ($Åk_{12}$) and melilite melt rather than CAI melt. Partition coefficients for Sr and Zr ($^{mel/melt}D_{Sr} = 0.78$, $^{mel/melt}D_{Zr} = 0.0010$ with undefined errors) agree well with our results (0.64–0.72(2) and 0.004(2), respectively). However, the partition coefficients for La, Sm, and Yb are much higher in the Kuehner et al. (1989) study ($^{mel/melt}D_{La} = 0.67$, $^{mel/melt}D_{Sm} = 0.75$, $^{mel/melt}D_{Yb} = 0.25$

with undefined error) than our measurements ($D_{La} = 0.052(1)$, $D_{Sm} = 0.073(1)$, $D_{Yb} = 0.017(1)$). If the difference in melilite composition is accounted for by $X_{Ge}/X_{Åk}$ (Beckett et al., 1990), the Kuehner et al. (1989) data would be 4.5× lower, in closer agreement with our results. Melt structure as well as significantly higher temperatures might account for the remaining differences with the Kuehner et al. (1989) study. The partition coefficients of Kuehner et al. (1989) are also "upper limits" according to the authors, due to the experimental and analytical techniques used.

In summary, although we have not performed any reversal experiments in this study, the homogeneity of both major and trace elements in the phases and the good agreement between experiments reflecting different time–temperature paths and doping levels and previous results argues that the measured partition coefficients represent a close approach to equilibrium.

4.2. Site size energetics model for partitioning

The structure of melilite consists of single and double tetrahedra containing Si, Al, and Mg arranged in sheets. The sheets are bonded together through Ca in distorted eightfold coordination. This structure results in three distinct cation sites: the X site, an eight coordination number site usually occupied by Ca; the T1 site, a larger tetrahedral site usually occupied by Al or Mg; and the smaller T2 site, a tetrahedral site usually occupied by Si or Al. The difference in these tetrahedral sites is shown by measured T–O bond lengths which exceed 1.9 Å in the T1 site while T–O bond lengths in the T2 site are less than 1.7 Å (Bindi et al., 2001). Spinel consists of two cation sites: an octahedral site containing Al and a tetrahedral site containing Mg. This crystallographic background forms the basis for understanding the partitioning behavior observed between both mineral phases and a coexisting CAI melt.

It has long been observed that log plots of partition coefficients (D_i) versus cation radii (r_i) for a series of isovalent cations produce parabolas with maxima corresponding to the size of the crystal lattice site(s) in which substitution occurs (Onuma et al., 1968). Blundy and Wood (1994), following the work of Brice (1975), developed a framework of site size energetics to describe and predict trace element partitioning based on this parabolic relationship. These authors showed that the partitioning of any series of isovalent cations is controlled by the size and elasticity of the crystal lattice sites into which the cations are substituting. They found that for an isovalent series of ions with charge $n+$ and radius r substituting into crystal lattice site M, the partition coefficient ($D_i(M)$) can be described in terms of three parameters: (1) $r_{0(M)}^{n+}$, the radius of that site; (2) E_M^{n+}, the elastic response of that site (Young's Modulus) to lattice strain caused by ions that are larger or smaller than $r_{0(M)}^{n+}$; and (3) $D_{0(M)}^{n+}$, the strain compensated partition coefficient for an ion with radius $r_{0(M)}^{n+}$, according to the expression:

$$D_i = D_{0(M)}^{n+}$$
$$\times \exp \left\{ \frac{-4\pi N_A E_M^{n+} \left[\frac{1}{2} r_{0(M)}^{n+} (r_i - r_{0(M)}^{n+})^2 + \frac{1}{3} (r_i - r_{0(M)}^{n+})^3 \right]}{RT} \right\}$$

(1)

where N_A is Avogadro's number (Blundy and Wood, 1994).

An important component of partitioning energetics upon which the above equation is based is the $\Delta G_{exchange}^{y-i}$, which is the free energy required to remove from the melt and insert into the crystal lattice a cation, i, differing in size and/or charge from cation y, and to simultaneously transfer y from crystal to melt. The $\Delta G_{exchange}^{y-i}$ is dominated by the strain energy around the mismatched cation in the crystal, linking the Young's Modulus of a crystal to the behavior of trace element partitioning (Blundy and Wood, 1994).

To determine the best fit parabola for an isovalent series in a given site, we linearly regressed the data plotted as $\left[\frac{1}{2} r_{0(M)}^{n+} (r_i - r_{0(M)}^{n+})^2 + \frac{1}{3} (r_i - r_{0(M)}^{n+})^3 \right]$ versus the natural log of the partition coefficients. The y-intercept of this line results in the optimum partition coefficient for the site ($D_{0(M)}^{n+}$) for a particular valence while the slope is directly proportional to the Young's Modulus of the site (E_M^{n+}) for that valence. We varied r_o to obtain the best fit as explained below.

Oversized cations, larger in radius than the optimum cation radius (r_o) of the melilite X site, are the easiest to interpret and give the most insight into bulk crystal properties. Our regressions for +1, +2, and +3 cations in the X site all produce well-correlated parabolic fits with ionic radius (Fig. 7). Because the parabola shape narrows with higher cation charge (Blundy and Wood, 1994), the +3 cations constrain the optimum radius (r_o) of the X site, with the maximum partition coefficient for the +3 rare earth elements (REE) occurring near Nd or Sm; thus the optimum radius for the X site is smaller than that of Ca (r_o of 1.10 Å
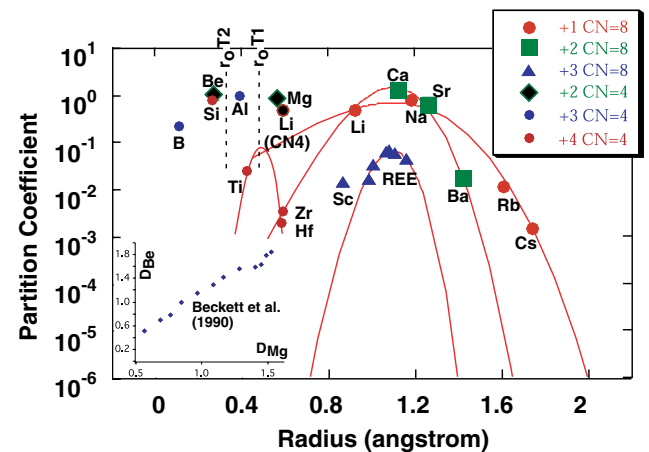

Fig. 7. Onuma diagram for trace elements partitioning between melilite and melt. Fit parabolas corresponding to the parameters given in Table 5 are shown. Ionic radii reflect values for CN = 8 and CN = 4 cations (Shannon, 1976). Inset at lower left shows correlation of DBe and DMg in experiments of Beckett et al. (1990).

vs. Ca^{2+} in $CN = 8$ of 1.14: Shannon, 1976). Ce is not included in this analysis because it is likely to be Ce^{4+}, given the $f(O_2)$ of these experiments.

We use the r_o value determined by the +3 cations for the site size energetics evaluation of +1 and +2 cations. The +2 cations Ca, Sr, and Ba, which can only substitute into the X site, produce a good fit with partition coefficients decreasing with increasing cation size. Similarly, the +1 cations Na, Rb, and Cs must also occupy the X site. Along with the $^{mel/melt}D_{Na}$ appropriate to our melilite composition from Beckett and Stolper (2000), our data produce a well constrained fit to the +1 parabola for the X site in melilite. The partition coefficient of Li indicates that it may be incorporated into this site; however its smaller size could also allow it to partition into the small T1 site; this will be discussed in more detail below.

The regression results for each isovalent series of cations entering the X site in melilite are given in Table 5. The E_M^{n+} of the X site changes considerably with heterovalent substitution, increasing with increasing ionic charge, as predicted by the Blundy and Wood (1994) model. For instance, the E_M^{n+} calculated for +1 substitution in the X site is only 324 kbar, while for +2 substitution it is 1049 kbar and for +3 substitution it is 2951 kbar. These values for E_M^{n+} are relatively similar to, but offset to lower values than typically observed for the M2 site in clinopyroxene which also contains Ca as the major cation (e.g., 504, 1465, and 3956 kbar, respectively in Blundy and Wood, 1994; 469–496, 1551–1645, and 2924–2979 kbar for Lundstrom et al., 1998). Furthermore, this value for E_M^{n+} of the +2 cations entering the X site is in good agreement with the minerals bulk modulus using crystallographic techniques as explained below.

Although the examples of oversized ions partitioning into the X site are straightforward, the treatment of an ion partitioning between a mineral and a melt becomes more complicated when the size of the ion falls between the size of two or more sites in the mineral, a case that applies to the light elements into melilite. In such a case, the ion would have separate partition coefficients for incorporation into each site which would in sum give the measured partition coefficient for the element. Furthermore, each cation has a different ionic radius depending on its coordination number, adding to the difficulty of predicting which site an element may partition into.

Table 5
Comparison of lattice site parameters estimated from partitioning data, with bulk crystal properties

	Charge	E (kbar)	D_O
X melilite site			
	1+	324	0.710
	2+[a]	1049	1.483
	3+	2951	0.070
Bulk crystal[b]		1067	

[a] Homovalent substitution.
[b] Li et al. (1990).

Given its ionic radius between that of the T1 and X sites, Li provides a good example of the difficulties associated with interpreting multiple site partitioning. Fig. 7 shows that $^{mel/melt}D_{Li}$ is consistent with the parabola predicted by other +1 cations into the X site. However, because cation radius decreases with decreasing coordination number, Li might also occupy the larger of the two tetrahedral sites, T1. Including Li in the +1 regression for the X site changes the E by 1% while the goodness of fit for the linear regressions with or without Li are both excellent ($R^2 > 0.99$ in both cases). If we assume that the goodness of fit with other +1 cations indicates an X site position for Li, then $^{mel/melt}D_{Li}$ should behave analogously to $^{mel/melt}D_{Na}$ being dependent on $X_{Åk}/X_{Ge}$ (Beckett and Stolper, 2000). On the other hand, if some Li partitions into the T1 site, then the increasing size of this site with increasing Mg likely means that $^{mel/melt}D_{Li}$ should increase with $X_{åk}$. Recent work by Ryerson et al. (2005) indicates that $^{mel/melt}D_{Li}$ changes only slightly with composition from ∼0.4 in Åk$_{50}$ melilite to ∼0.53 in Åk$_{100}$ melilite. This small range/lack of compositional dependence is consistent with the low E_M^{n+} of +1 cations substituting into a given site. Given the small spread in melilite composition in our experiments, we cannot definitively describe the changes in Li partitioning with composition but argue that little variation should occur.

The dependence of Be partitioning on melilite composition has already been established by the work of Beckett et al. (1990) which showed that $^{mel/melt}D_{Be}$ varied regularly from 0.53 at Åk$_{29}$ to 1.86 at Åk$_{75}$ (inset shown in Fig. 7). Although the correlation between $^{mel/melt}D_{Mg}$ and $^{mel/melt}D_{Be}$ might seem to imply Be follows Mg into the same T1 site in melilite, analysis of Be substitution from a site size energetics approach suggests that Be probably enters the T2 site. The radius of tetrahedrally coordinated Be^{2+} (0.27 Å) is almost identical to that of Si^{4+} (0.26 Å), yet significantly smaller than that of Mg^{2+} (Shannon, 1976). The correlation between $^{mel/melt}D_{Mg}$ and $^{mel/melt}D_{Be}$ (Beckett et al., 1990) supports Be entering the T2 site rather than the T1 site. As the akermanite content of melilite increases, the optimum radius (r_o) of the T1 and T2 sites will become more different as less aluminum partitions into each site. In other words, the T1 site size becomes larger with increasing Mg content while the T2 site size shrinks with increasing Si content. As the T2 site size approaches that of Si, it becomes more amenable to Be incorporation while the T1 site becomes less amenable. Our analysis of +4 cation partitioning into the T1 site corroborates this interpretation as the best fit r_o for a parabola constrained by Ti, Zr, and Hf partition coefficients is 0.44 Å. This r_o agrees qualitatively with expectation of the r_o of the T1 site being between that of tetrahedral Mg^{2+} (0.57 Å) and Al^{3+} (0.39 Å) and much larger than the radius of Be^{2+} (0.27 Å, Shannon, 1976).

The partitioning of B is consistent with prediction based on knowledge of the B^{3+} ion's size relative to the smallest cation site in melilite, the T2 site. Fig. 7 shows that

CN = 4 B^{3+} cation is dramatically smaller than even Si^{4+} which represents the minimum size of the T2 site; as more Al enters this site with increasing gehlenite component, the average T2 site size will become larger, making B even more incompatible. The tighter parabola of +3 cations means that changes in site size have greater effect such that B is likely to be highly incompatible in gehlenitic melillite. Ryerson et al. (2005) report that $^{mel/melt}D_B$ is 0.18 in $Åk_{50}$ (similar to our result) but is only 0.05 in $Åk_{100}$, opposite to this prediction. The reason for this mismatch between model and observation is not understood but the bottom line of both model prediction and experimental observation is that B is highly incompatible and will therefore be enriched in the melt during progressive crystallization.

As noted by Blundy and Wood (1994), when cations with the same valence as the major element occupying a site substitute into a large cation site, the Young's Modulus (E_M^{n+}) calculated from the isovalent series is similar in value to the Young's Modulus (E) for the bulk crystal. This relationship implies that the elastic properties of the crystal are strongly influenced by the elastic properties of the large cation site, rather than by the relatively rigid tetrahedral framework (Blundy and Wood, 1994). In this light, the Young's modulus indicated by our X site regression for +2 cations is in excellent agreement with the bulk crystal properties of åkermanite determined by X-ray diffraction methods (Table 5) (Li et al., 1990). For instance, the E_M^{n+} for the X site in melilite calculated from the +2 partition coefficients determined in this study is 1049 kbar, which compares favorably to the measured Young's Modulus of åkermanite, 1067 kbar (Li et al., 1990). The conclusion that the elastic properties of the X site control the bulk crystal is also consistent with the interpretation of Li et al. (1990) that the silica tetrahedra act as nearly rigid groups in melilite, with the response to stress being mainly through tetrahedral rotation (a change in the Mg–O–Si and Si–O–Si angles). However, the large X site with relatively weak ionic bonds is much softer and can accommodate stress through compression of cation-O bonds in addition to O-cation-O bond bending. Li et al. (1990) posit that the replacement of T1 and T2 cations by other tetrahedral cations has relatively little effect on the elastic moduli of the melilite structure, whereas substantial changes would be expected if Ca^{2+} were replaced by a smaller or larger cation of differing valence. Thus, the occurrence of significant amounts of Na in the X site as occurs in terrestrial igneous melilites is likely to significantly change the Young's modulus and hence partitioning of oversized cations in the igneous situation relative to the CAI application discussed here.

4.3. Application of the partition coefficients to the Li–Be–B distribution in CAI

Prerequisites for the existence of an isochron-like relationship between $^{10}B/^{11}B$ and $^{9}Be/^{11}B$ (^{10}Be radioactive decay into ^{10}B) or between $^{7}Li/^{6}Li$ and $^{9}Be/^{6}Li$ (^{7}Be radioactive decay into ^{7}Li) in CAIs are that the Li and B isotopic compositions were once homogenized, that $^{9}Be/^{11}B$ and $^{9}Be/^{6}Li$ ratios were subsequently fractionated and that the CAI evolved as a closed system. The chronological meaning of the slopes of the ^{10}Be isochron depends on the process by which Be was fractionated relative to B. For instance, if the $^{9}Be/^{11}B$ variations reflect crystal fractionation of the CAI parent melt, then the slope of the ^{10}Be isochron dates the time of differentiation and crystallization of the CAI. The partition coefficient data provided by this and previous studies allow assessment of processes responsible for creating the observed chemical fractionations between the light elements. Consistency between observed variations and crystallization models establish whether or not magmatic processes may have created the element distribution. However, many CAIs have clearly undergone complex histories including multiple events of re-heating and/or alteration after a possibly igneous process of formation (MacPherson, 2004). Knowledge of the expected nuclide distribution based on partitioning can be useful to identify zones in a CAI where the short-lived radionuclide abundances may have been perturbed. This aspect is especially important in the case of Li and B. In fact, although these two elements are not refractory, their distribution in CAIs suggests that they were partitioned locally during magmatic processes, implying that they were introduced at a late stage in the CAI melt (Chaussidon et al., 2006).

Our application is focused on type B inclusions because these are generally considered to result from crystallization from a melt (MacPherson and Grossman, 1981; Wark and Lovering, 1982). Specifically, we examine models to explain the variations in Li–Be–B observed within one type B CAI from Allende (CAI 3529-41, Podosek et al., 1991; Chaussidon et al., 2004; Chaussidon et al., 2006). This inclusion was chosen despite its mineralogical and geochemical complexity because it contained at its time of formation some of the highest levels of ^{26}Al (Podosek et al., 1991) and ^{10}Be (McKeegan et al., 2000) observed in CAIs. CAI 3529-41 is presently the only CAI in which the Li–Be–B concentrations and the Li and B isotopic ratios have been studied in detail. The major mineral phases in CAI 3529-41 (anorthite, fassaite, and anorthite) show a very well defined ^{10}Be isochron indicating a $^{10}Be/^{10}B$ of $8.8 \pm 0.6 \times 10^{-4}$ at the time of crystallization (Chaussidon et al., 2006). From the experimentally determined partitioning of Be in melilite (Beckett et al., 1990), it is possible to identify in the melilites of CAI 3529-41 zones where the Be concentrations follow closed system magmatic partitioning. In these zones, the $^{7}Li/^{6}Li$ ratios are positively correlated with the $^{9}Be/^{6}Li$ ratios in a manner indicating the in situ decay of radioactive ^{7}Be with an initial $^{7}Be/^{9}Be$ ratio of $6.1 \pm 1.3 \times 10^{-3}$ (Chaussidon et al., 2006). All the zones in CAI 3529-41 in which perturbation of the magmatic Be distribution was indicated by deviation from the expected [Be] vs Åk relationship (Fig. 4 in Chaussidon et al., 2006) show homogeneous $^{7}Li/^{6}Li$ ratios, interpreted to reflect post-magmatic re-homogenization of Li isotopes after ^{7}Be was extinct.

Because of the very short half-life of ^{7}Be (53 days), the ^{7}Be/^{7}Li system is very sensitive to such post-magmatic perturbations. Here, we examine whether the present Li–Be–B partitioning data between melilite, spinel, and CAI melt can help to further constrain the process which controlled the Li–Be–B distributions in CAI 3529-41.

Fig. 8 shows the Li–Be–B concentrations measured in melilites from 3529-41, along with several progressively more complicated models of closed system fractional crystallization from a CAI melt. By increasing the relative complication of the models, we can determine the most important controls and largest uncertainties in relating the experimental measurements to observed light element variations in CAIs. We assume initial bulk Li, Be, and B concentrations in the CAI melt of 15 ppb, 50 ppb and 15 ppb, respectively. For comparison, the average melilite
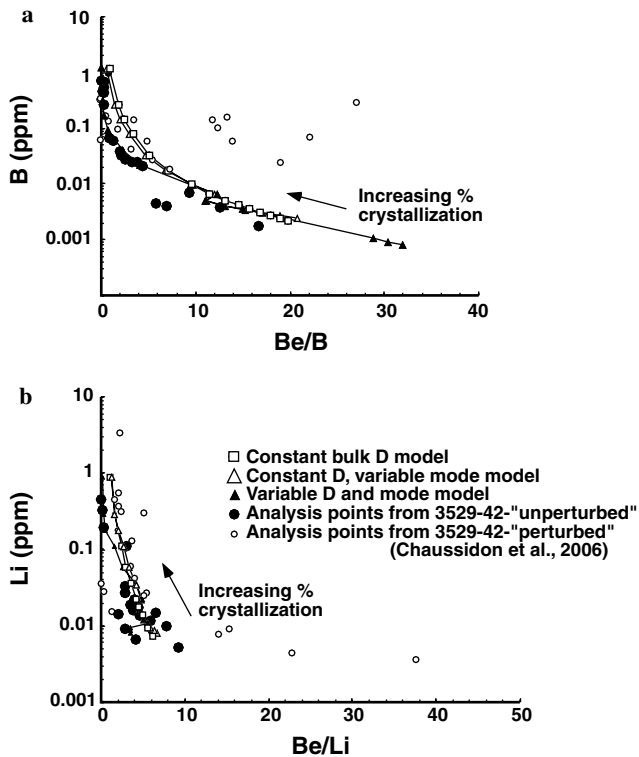
Fig. 8. Trace element variation diagrams for the light elements in melilites (a) Be–B vs B; (b) Be–Li vs Li. Closed circles show melilite analyses by SIMS of spots in Allende CAI 3529-41 that have been designated unperturbed based on the behavior of Be concentration relative to the melilite composition (see Chaussidon et al. (2006) for details; inclusion 3529-41 is described in Podosek et al., 1991). Open circles show spots in 3529-41 which are interpreted to have had their light element abundances affected by secondary processes. Lines show the results for three fractional crystallization models using the partition coefficients determined in this study (see text and Table 6 for details of partition coefficients used; F, fraction of melt remaining, varies from 0.9 to 0.001). Filled circles show simple constant bulk partition coefficient model. Open triangles show three stage model involving changing mode but constant partition coefficient in each phase. Filled triangles show changing mode and partition coefficient model. Note the absence of any observational data consistent with early spinel only crystallization (initial trend in variable mode models). Note also the good correspondence between the data and all of the model trends at advanced stages of crystallization (F < 0.5).

concentration for each of these elements in 3529-41 is ≈170 ppb, ≈500 ppb, and ≈190 ppb while the average fassaite and anorthite contents are ≈10 ppb, ≈40 ppb, and ≈150 ppb, respectively (Chaussidon et al., 2006). Thus, given melilite modes of >10%, our assumed initial concentrations for the models may be too low. Changing the starting concentrations to higher values would simply shift the curves in Figs. 8a and b upward.

For the simplest model, we assume a constant bulk partition coefficient for each element. Assuming that the modes of the crystallizing phases are 10% spinel, 60% melilite, and 30% of other silicates (pyroxene and/or feldspar) throughout crystallization, we arrive at the following bulk partition coefficients based on our results along with partitioning data for aluminous clinopyroxene from Ryerson et al. (2005): $D_{Li}^{CAI/melt} = 0.298$, $D_{Be}^{CAI/melt} = 0.548$, and $D_B^{CAI/melt} = 0.095$ (Table 6). Plagioclase partition coefficients could also be included in the calculation but replacing clinopyroxene with plagioclase does not drastically change the result given the low and similar values of the light element partition coefficients for these two phases (Ryerson et al. (2005)). This model reproduces the general trends of the light elements observed in 3529-41.

Next, we incorporate the more realistic effect of changing mineral mode with progressive crystallization as outlined by the experiments of Stolper (1982). Specifically, we develop a three stage model whereby the first stage reflects 10% crystallization of spinel only, the second stage reflects 50% crystallization of melilite plus spinel (proportions 90% melilite and 10% spinel), and the third and final stage (last 40% crystallization) reflects melilite, pyroxene, and spinel (in 60–30–10% proportions, respectively) using the same constant partition coefficients for each phase. Results for this model are essentially indistinguishable from the first model. The model predicts that spinels crystallized from an initial homogeneous melt would have fundamentally different compositional trends from those co-crystallizing with melilite. Thus, analysis of light element concentrations within spinels could provide an important test for finding evidence for CAI crystallization from an initially homogeneous melt. Unfortunately, this aspect is difficult to test at present because spinels in CAIs are often of small size (20 μm or less) compared to the size of the ion probe primary beam.

Finally, we add the realism of changing partition coefficients and modes with progressive crystallization, using compositional constraints from our results and the results of Beckett et al. (1990). We model this incrementally in seven steps changing partition coefficients throughout the crystallization sequence (Table 6). In our calculation, $^{mel/melt}D_{Be}$ ranges from 0.5 for $X_{Ak} = 0.3$ to 1.9 for $X_{Ak} = 0.75$ (Beckett et al., 1990). Based on our arguments above and observations from Ryerson et al. (2005), we assume $^{mel/melt}D_{Li}$ to be constant over the crystallization interval while $^{mel/melt}D_B$ changes only slightly. Results of this model show only small deviations from the previous models indicating that constant partition coefficient models

Table 6
Parameters used in fractional crystallization models

	Spinel	Melilite	Pyroxene[*]
Constant partition coefficients used in models 1 and 2:			
$D_{Li}=$	0.1	0.477	0.007
$D_{Be}=$	0.04	0.881	0.05
$D_B=$	0.003	0.148	0.02

	Bulk	Spinel	Melilite	Pyx
Partition coefficients and modes used in model 3:				
Stage 1-sp only				
$D_{Li}=$	0.100	0.1		
$D_{Be}=$	0.040	0.04		
$D_B=$	0.003	0.003		
Stage 2-Åk₂₅; 10% sp + 90% mel.				
$D_{Li}=$	0.439	0.1	0.477	
$D_{Be}=$	0.454	0.04	0.5	
$D_B=$	0.045	0.003	0.05	
Stage 3-Åk₄₀; 10% sp + 90% mel.				
$D_{Li}=$	0.439	0.1	0.477	
$D_{Be}=$	0.904	0.04	1.0	
$D_B=$	0.135	0.003	0.15	
Stage 4-Åk₅₀; 10% sp + 60% mel. + 30% pyx				
$D_{Li}=$	0.298	0.1	0.477	0.007
$D_{Be}=$	0.739	0.04	1.2	0.05
$D_B=$	0.096	0.003	0.15	0.02
Stage 5-Åk₆₀; 10% sp + 60% mel. + 30% pyx				
$D_{Li}=$	0.298	0.1	0.477	0.007
$D_{Be}=$	0.919	0.04	1.5	0.05
$D_B=$	0.126	0.003	0.2	0.02
Stage 6-Åk₇₀; 10% sp + 60% mel. + 30% pyx				
$D_{Li}=$	0.298	0.1	0.477	0.007
$D_{Be}=$	1.099	0.04	1.8	0.05
$D_B=$	0.126	0.003	0.2	0.02

are likely adequate in distinguishing first order effects of crystallization.

Two conclusions can be drawn from the comparison of these models with the observational data: first, all of the models reproduce the trends in Li–Be–B distribution observed in 3529-41 reasonably well (Figs. 8a and b), particularly for the latter stages of crystallization. Both Be–B and Be–Li in the initial stages of the models fail to match the observed ratios. If higher initial Be–B or Be–Li are used, the trends of the majority of the data are not matched. Second, the increased complexity of variable modes and partition coefficients does not lead to different results between the models; indeed, the simplest constant bulk partition coefficient model produces similar conclusions as the more complex models, that the trend within advanced stages of crystallization reproduce the observations fairly well.

In addition, the model reproduces the trends in Li–Be–B concentrations and ratios observed for the "unperturbed" zones in melilites (Figs. 8a and b). These zones were previously identified as reflecting a magmatic partitioning trend (solid circles in Figs. 8a and b) based their [Be] versus Åk variations (Chaussidon et al., 2006). In contrast, zones which were identified as showing clear post-magmatic

perturbations of their Be distributions (open circles in Figs. 8a and b) plot significantly away from the differentiation trends modeled using the present Li–Be–B partitioning data. This observation adds support to the idea that the Li–Be–B distributions in CAI 3529-41 can be broadly categorized as perturbed and unperturbed, with magmatic distributions preserved in unperturbed areas; these are locations where the signs of [7]Be decay can be looked for. Note that the range in Be–Li, found in the lowest concentration analytical points, cannot be explained by either spinel or melilite partitioning (the two possible phases crystallizing early from a CAI melt). Thus, the cause of the large and "non magmatic" variations of Li–Be–B concentration in some zones of the melilite crystals remain enigmatic, especially because they do not appear to reflect late alteration processes (Chaussidon et al., 2006). Whatever their cause, the present data show however that they can be identified from simple models of crystal fractionation of a CAI melt.

5. Conclusions

We report melilite–melt and spinel–melt partition coefficients for 21 trace elements at one atmosphere pressure and

cooling rates appropriate to the formation of CAIs. Partition coefficients for three separate experiments at different trace element doping levels are in excellent agreement indicating a close approach to equilibrium and Henry's law behavior. Furthermore, partition coefficient measurements show agreement between SIMS and LA-ICP-MS analyses as well as agreement with previous studies of melilite–melt partitioning.

A site size energetics analysis indicates systematic behavior for trace element partitioning as a function of ionic radius into the large X site occupied by Ca in melilite. The Young's Modulus of the X site obtained by regression of the +2 cation partitioning agrees well with the bulk modulus of åkermanite determined by X-ray methods (Li et al., 1990).

Using our measured partition coefficients along with literature values for other crystallizing phases, we evaluate if observed Li, Be, and B systematics in CAI 3529-41 from Allende can be explained by models of fractional crystallization of a melt. Models of fractional crystallization using these partition coefficients result in good reproduction of light element concentration trends within "unperturbed" portions of CAI3529-41.

Acknowledgments

Associate editor: Alexander N. Krot

References

Amelin, Y., Krot, A.N., Hutcheon, I.D., Ulyanov, A.A., 2002. Lead isotopic ages of chondrules and calcium–aluminum-rich inclusions. *Science* **297**, 1678–1683.

Beckett, J.R., Spivack, A.J., Hutcheon, I.D., Wasserburg, G.J., Stolper, E.M., 1990. Crystal chemical effects on the partitioning of trace elements between mineral and melt; an experimental study of melilite with applications to refractory inclusions from carbonaceous chondrites. *Geochim. Cosmochim. Acta* **54**, 1755–1774.

Beckett, J.R., Simon, S.B., Stolper, E., 2000. The partitioning of Na between melilite and liquid; Part II, Applications to Type B inclusions from carbonaceous chondrites. *Geochim. Cosmochim. Acta* **64**, 2519–2534.

Beckett, J.R., Stolper, E., 2000. The partitioning of Na between melilite and liquid; Part I, The role of crystal chemistry and liquid composition. *Geochim. Cosmochim. Acta* **64**, 2509–2517.

Bindi, L., Bonazzi, P., Dusek, M., Petricek, V., Chapuis, G., 2001. Five-dimensional structure refinement of natural melilite, (Ca1.89, Sr0.01, Na0.08, K0.02) (Mg0.92, Al0.08)–(Si1.98, Al0.02)O7. *Acta Crystallogr. B* **57**, 739–746.

Blundy, J., Wood, B., 1994. Prediction of crystal–melt partition coefficients from elastic moduli. *Nature* **372**, 452–454.

Botazzi, P., Ottolini, L., Vannucci, R., 1992. SIMS analyses of REE in natural minerals and glasses: an investigation of structural matrix effects on ion yields. *Scan. Electron Microsc.* **14**, 160–168.

Brice, J.C., 1975. Some thermodynamic aspects of the growth of strained crystals. *J. Cryst. Growth* **28**, 249–253.

Chaussidon, M., Gounelle, M., 2006. Irradiation processes in the early solar system. In: Lauretta, D., Leshin, L. (Eds.), *Meteorites and the early solar system II*. Arizona University press, pp. 323–339.

Chaussidon, M., Robert, F., McKeegan K.D., 2004. Li and B isotopic variations in Allende type B1 CAI 3529-41: traces of incorporation of short-lived [7]Be and [10]Be. *Lunar Planet. Sci. XXXV*. Lunar Planet. Inst., Houston. #1568 (abstract).

Chaussidon, M., Robert, F., McKeegan, K.D., 2006. Li and B isotopic variations in an Allende CAI: evidence for the in situ decay of short-lived [10]Be and for the possible presence of the short-lived nuclide [7]Be in the early solar system. *Geochim. Cosmochim. Acta* **70**, 224–245.

Chen, J., Wasserburg, G.J., 1981. The isotopic composition of Uranium and lead in Allende inclusions and meteorite phosphates. *Earth Planet. Sci. Lett.* **52**, 1–15.

Connolly, H.C., Burnett, D.S., McKeegan, K.D., 2003. The petrogenesis of type B1 Ca-Al-rich inclusions: the spinel perspective. *Meteorit. Planet. Sci.* **38**, 197–224.

Davis, A.M., Richter, F.M., Simon, S.B., Grossman, L., 1996. The effect of cooling rate on melilite/liquid partition coefficients for Y and REE in Type B CAI melts. *Lunar Planet. Sci. XXVII*. Lunar Planet. Inst., Houston, 291–292.

Desch, S.J., Connolly, H.C., Srinivasan, G., 2004. An interstellar origin for the beryllium-10 in calcium-rich, aluminum-rich inclusions. *Astrophys. J.* **602**, 528–542.

Gilletti, B.J., Shanahan, T.M., 1997. Alkali diffusion in plagioclase feldspar. In: Hawkesworth, C., Arndt, N. (Eds.), *Highlights of the Goldschmidt Meeting, in Honor of A.W. Hofmann*, 139. Elsevier, Amsterdam, pp. 3–20.

Grossman, L., 1975. Petrography and mineral chemistry of Ca-rich inclusions in the Allende meteorite. *Geochim. Cosmochim. Acta* **39**, 433–454.

Kennedy, A.K., Beckett, J.R., Edwards, D.A., Hutcheon, I.D., 1997. Trace element disequilibria and magnesium isotope heterogeneity in 3655A: Evidence for a complex multi-stage evolution of a typical Allende type B1 CAI, Geochim. *Cosmochim. Acta* **61**, 1541–1561.

Kuehner, S.M., Laughlin, J.R., Grossman, L., Johnson, M.L., Burnett, D.S., 1989. Determination of trace element mineral/liquid partition coefficients in melilite and diopside by ion and electron microprobe techniques. *Geochim. Cosmochim. Acta* **53**, 3115–3130.

Lee, T., Papanatassiou, D.A., Wasserburg, G.J., 1976. Demonstration of [26]Mg excess in Allende and evidence for [26]Al. *Geophys. Res. Lett.* **3**, 109–112.

Li, Z., Chan, S.-K., Ghose, S., 1990. Elastic properties of the incommensurate phase of åkermanite, Ca2MgSi2O7. *Phys. Chem. Miner.* **17**, 462–466.

Lundstrom, C.C., Shaw, H.F., Ryerson, F.J., Williams, Q., Gill, J., 1998. Crystal chemical control of clinopyroxene-melt partitioning in the Di-Ab-An system: implications for elemental fractionations in the depleted mantle. *Geochim. Cosmochim. Acta* **62**, 2849–2862.

MacPherson, G.J., 2004. Calcium–Aluminum-rich inclusions in chondritic meteorites. In: Davis, A.M. (Ed.), *Treatise of Geochemistry*, vol. 1. Elsevier, Amsterdam, pp. 201–246.

MacPherson, G.J., Davis, A.M., 1993. A petrologic and ion microprobe study of a Vigarano Type B2 refractory inclusion: evolution by multiple stages of melting and alteration. *Geochim. Cosmochim. Acta* **57**, 231–243.

MacPherson, G.J., Grossman, L., 1981. A once-molten, coarse-grained, Ca-rich inclusion in Allende. *Earth Planet. Sci. Lett.* **52**, 16–24.

MacPherson, G.J., Huss, G.R., Davis, A.M., 2003. Extinct [10]Be in type A calcium–aluminum-rich inclusions from CV chondrites. *Geochim. Cosmochim. Acta* **67**, 3165–3179.

Mason, B., Martin, P.M., 1974. Minor and trace element distribution in melilite and pyroxene from the Allende meteorite. *Earth Planet. Sci. Lett.* **22**, 141–144.

McKeegan, K.D., Chaussidon, M., Robert, F., 2000. Incorporation of short-lived [10]Be in a calcium–aluminum-rich inclusion from the Allende Meteorite. *Science* **289**, 1334–1337.

Onuma, N., Higuchi, H., Wakita, H., Nagasawa, H., 1968. Trace element partition between two pyroxenes and the host lava. *Earth Planet. Sci. Lett.* **5**, 47–51.

Podosek, F.A., Zinner, E.K., MacPherson, G.J., Lundberg, L.L., Brannon, J.C., Fahey, A.J., 1991. Correlated study of initial 87Sr/86Sr and Al–Mg isotopic systematics and petrologic properties in a suite of refractory inclusions from the Allende Meteorite. *Geochim. Cosmochim. Acta* **55**, 1083–1110.

Ryerson, F.J., Brenan, J.M., Phinney, D.L., 2005. Experimental determination of Li, Be, and B partitioning during CAI crystallization. *Lunar Planet. Sci. XXXVI*, Lunar Planet. Inst., Houston, 1531–1532.

Shannon, R.D., 1976. Revised effective ionic radii and systematic studies of inter-atomic distances in halides and chalcogenides. *Acta Crystallogr.* **A32**, 751–767.

Shimizu, N., Semet, M.P., Allegre, C.J., 1978. Geochemical applications of quantitative ion-microprobe analysis. *Geochim. Cosmochim. Acta* **42**, 1321–1334.

Simon, S.B., Grossman, L., Davis, A.M., 1991. Fassaite composition trends during crystallization of Allende Type B refractory inclusion melts. *Geochim. Cosmochim. Acta* **55**, 2635–2655.

Stolper, E.M., 1982. Crystallization sequences of Ca–Al-rich inclusions from Allende; an experimental study. *Geochim. Cosmochim. Acta* **46**, 2159–2180.

Stolper, E., Paque, J.M., 1986. Crystallization sequences of Ca–Al-rich inclusions from Allende; the effects of cooling rate and maximum temperature. *Geochim. Cosmochim. Acta* **50**, 1785–1806.

Sugiura, N., Shuzou, Y., Ulyanov, A.A., 2001. Beryllium–boron and aluminum–magnesium chronology of calcium–aluminum-rich inclusions in CV chondrites. *Meteorit. Planet. Sci.* **36**, 1397–1408.

Tilton, G.W., 1988. Age of the solar system. In: Kerridge, J.F., Mathews, M.S. (Eds.), *Meteorites and the Early Solar System*, pp. 259–275.

Wark, D.A., 1979. Birth of the pre-solar Nebula—Sequence of condensation revealed in the Allende Meteorite. *Astrophys. Space Sci.* **65**, 275–295.

Wark, D.A., Lovering, J.F., 1982. The nature and origin of type B1 and B2 Ca–Al-rich inclusions in the Allende Meteorite. *Geochim. Cosmochim. Acta* **46**, 2581–2594.

Wark, D.A., Boynton, W.V., Keays, R.R., Palme, H., 1987. Trace element and petrologic clues to the formation of forsterite-bearing Ca–Al-rich inclusions in the Allende meteorite. *Geochim. Cosmochim. Acta* **51**, 607–622.

Watson, E.B., 1985. Henry's law behavior in simple systems and magmas: criteria for discerning concentration-dependent partition coefficients in nature. *Geochim. Cosmochim. Acta* **49**, 917–923.